

Monitoring Oxygen Movement by Raman Spectroscopy of Resistive Random Access Memory with a Graphene-Inserted Electrode

He Tian,^{†,‡,⊥} Hong-Yu Chen,^{§,⊥} Bin Gao,^{§,||} Shimeng Yu,[§] Jiale Liang,[§] Yi Yang,[†] Dan Xie,[†] Jinfeng Kang,^{||} Tian-Ling Ren,^{*,†} Yuegang Zhang,^{*,‡,§} and H.-S. Philip Wong^{*,§}

[†]Institute of Microelectronics and Tsinghua National Laboratory for Information Science and Technology (TNList), Tsinghua University, Beijing 100084, China

[‡]The Molecular Foundry, Lawrence Berkeley National Laboratory, 1 Cyclotron Road, Berkeley, California 94720, United States

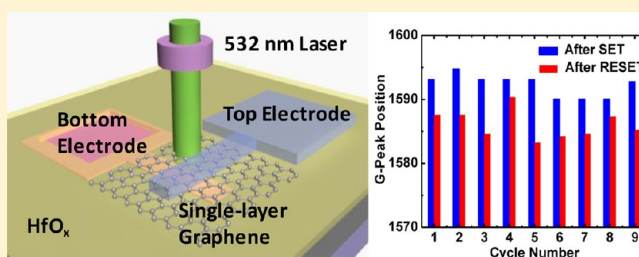
[§]Center for Integrated Systems and Department of Electrical Engineering, Stanford University, Stanford, California 94305, United States

^{||}Institute of Microelectronics, Peking University, Beijing 100871, China

S Supporting Information

ABSTRACT: In this paper, we employed Raman spectroscopy to monitor oxygen movement at the electrode/oxide interface by inserting single-layer graphene (SLG). Raman area mapping and single-point measurements show noticeable changes in the D-band, G-band, and 2D-band signals of the SLG during consecutive electrical programming repeated for nine cycles. In addition, the inserted SLG enables the reduction of RESET current by 22 times and programming power consumption by 47 times. Collectively, our results show that monitoring the oxygen movement by Raman spectroscopy for a resistive random access memory (RRAM) is made possible by inserting a single-layer graphene at electrode/oxide interface. This may open up an important analysis tool for investigation of switching mechanism of RRAM.

KEYWORDS: Graphene, resistive random access memory, oxygen ions movement, Raman spectroscopy, filaments



Metal oxide resistive random access memory (RRAM)¹ is one of the most promising candidates for emerging nonvolatile memory.^{2–10} Understanding the dynamics of resistive switching is of critical importance to realizing the promise of RRAM as a practical technology. Although the formation of conducting filaments has been visualized in several device/material systems,^{11–15} these results only provided the rudimentary information of whether filaments exist or not in the on- and off-states. Questions crucial to understanding the formation of the conducting filaments, such as how the filament begins to grow during the SET process and how the conducting channel is disconnected during the RESET process, remain uncertain. The commonly accepted theory to explain the formation of the conducting filament in RRAM switching is based on oxygen ions movement.¹⁶ The oxygen ions migrate from the oxide to the anode (top electrode) under the presence of electric field, which would leave oxygen vacancy to form conducting filaments and make the resistance of oxide change from high to low. The oxygen ions migrate from the top electrode back to the oxide under the reverse electric field, which would fill oxygen vacancy and make the resistance change from low to high. Although it is proposed that oxygen-related defects are responsible for the formation of the conducting filaments in RRAM,^{17–19} the migration of oxygen ions has not been fully studied yet.

In this work, we integrate single-layer graphene (SLG) into RRAM to investigate its resistance switching mechanism. Graphene has attracted much attention due to its outstanding material properties²⁰ such as ultrahigh carrier mobility,²¹ extremely high mechanical strength,²² and ultrahigh thermal conductivity²³ and transparency.²⁴ On the basis of those properties, graphene has been widely investigated for various applications.^{25,26} Graphene has previously been used for memory devices mainly as the electrode²⁷ or the resistive switching layer;²⁸ yet there is no report to date on the use of SLG as an interfacial layer to monitor oxygen movement in RRAM.

In this study, we insert SLG into the electrode/oxide interface of RRAM to monitor the oxygen movement by Raman spectroscopy. SLG could be used as an “oxygen barrier” to prevent oxygen ions from further migrating deep into the metal electrode. We monitor the migration of oxygen ions using electrical measurement coupled with Raman spectroscopy. Raman area mapping and single-point measurement show noticeable changes in the D-band, G-band and 2D-band signals of the SLG during electrical cycling. Because of the high out-of-

Received: November 16, 2012

Revised: December 28, 2012

Published: January 2, 2013

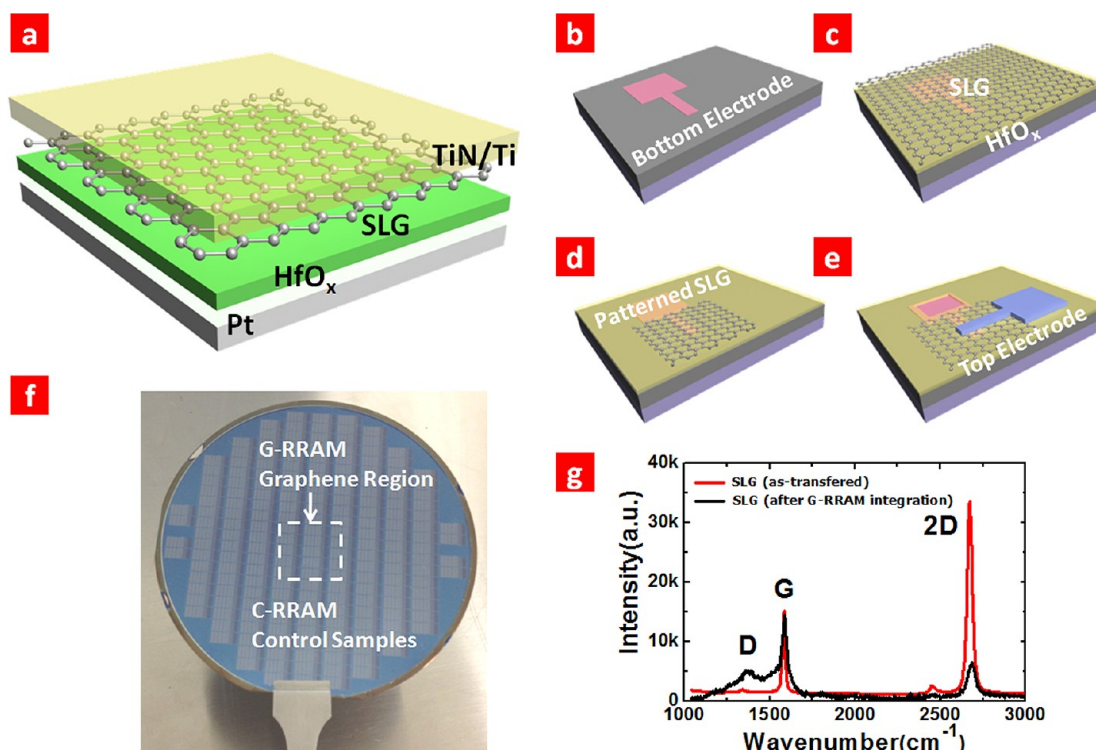


Figure 1. G-RRAM structure and fabrication process. (a) Schematic structure of G-RRAM. SLG is inserted between the top electrode (TiN/Ti ~ 70 nm) and the metal oxide layer ($\text{HfO}_x \sim 5$ nm). (b–e) Main process flow of G-RRAM. (f) A photograph of G-RRAM (with graphene) and C-RRAM (without graphene, control sample) arrays on a 4 in. wafer. (g) Raman data of as-transferred and after G-RRAM integration.

plane resistance of SLG and the high interfacial resistance of the SLG/oxide interface,⁹ Joule heating is effectively generated at the graphene/oxide interface. The high resistance introduced by SLG reduces reset current for RRAM, which offers a potential path toward further ultralow programming energy for RRAM.

Figure 1a shows a schematic illustration of the HfO_x -based RRAM devices with inserted SLG (G-RRAM). In this structure, the SLG is inserted between HfO_x and the top electrode. In order to make comparison, control samples without graphene (C-RRAM) were also fabricated. Figure 1b–e shows the device fabrication process (see Supporting Information Methods). Figure 1f shows the G-RRAM and C-RRAM arrays on a 4 in. wafer. The Raman spectrum (the red line) in Figure 1g confirms that the good quality of as-grown SLG is preserved after it is transferred onto the substrate. The G-peak position is at 1584 cm^{-1} , which indicates that the transferred graphene is very close to intrinsic undoped graphene (typically at $1583 \pm 1\text{ cm}^{-1}$).²⁹ The black line shows the D-peak intensity increases significantly after the full device integration process is completed. The D peak is mainly related to the defects in graphene, which may be introduced during the device fabrication (such as TiN sputtering). It is also noticed that the 2D peak decreases significantly after the G-RRAM integration (top process shown in Figure 1d,e). This is mainly related to the doping effect in graphene. H_2O could be a p-type dopant³⁰ introduced during the clean process of using deionization water in Figure 1e. In G-RRAM, the introduction of doping may also result from the oxygen plasma patterning in Figure 1d. The oxygen ions may stay at the edge of the graphene after the oxygen plasma patterning, which could function as a p-type dopant.³⁰ The presence of oxygen could decrease the 2D peak significantly.

As the Raman scattering is an effective way to characterize the structural information of graphene, a Raman microscope coupled with SLG could be used to probe the changes inside the RRAM during the cycling. G-RRAM with crossbar top and bottom electrodes is shown in Figure 2a. SEM images of $0.5 \times 0.5\text{ }\mu\text{m}^2$ cross-point region inside the $10 \times 10\text{ }\mu\text{m}^2$ SLG under low magnification and high magnification are shown in Figure 2b,c, respectively. Figure 2d shows the optical image of a G-RRAM device. The $0.5 \times 0.5\text{ }\mu\text{m}^2$ cross-point region is the active RRAM device. The area of SLG is $10 \times 10\text{ }\mu\text{m}^2$, which consists of the $0.5 \times 0.5\text{ }\mu\text{m}^2$ active region and the $99.75\text{ }\mu\text{m}^2$ nonactive region. In the Raman area mapping photographs (Figure 2e–j), the relatively light-colored areas represent the strong Raman intensity and relatively dark colored areas represent the weak Raman intensity. Figure 2e shows the G-band area mapping of the graphene. The light area shows the entire area of $10 \times 10\text{ }\mu\text{m}^2$ covered by graphene. The results of Raman D-band area mapping after SET/RESET programming cycles are shown in Figure 2f–j. As shown in Figure 2f, it is obvious that the D-band intensity is quite strong for the virgin device before any programming. After the SET/RESET programming cycles, the D-band intensity decrease gradually (Figure 2g–j) and we can find the increase of dark area in the Raman area map.

Figure 3a shows single-point Raman measurements over nine cycles of SET/RESET programming at the same location, which is $1\text{ }\mu\text{m}$ from the cross point. The gradual decrease of D peak in Figure 3b is consistent with the observations in Figure 2f–j. For G-RRAM, we also observed reversible shifts of G peak position after RRAM programming operations (Figure 3c). Figure 3d shows the intensity of 2D peak as a function of switching cycle. The 2D peak intensity of SET is always lower than the peak intensity of RESET in each cycle, and a reversible

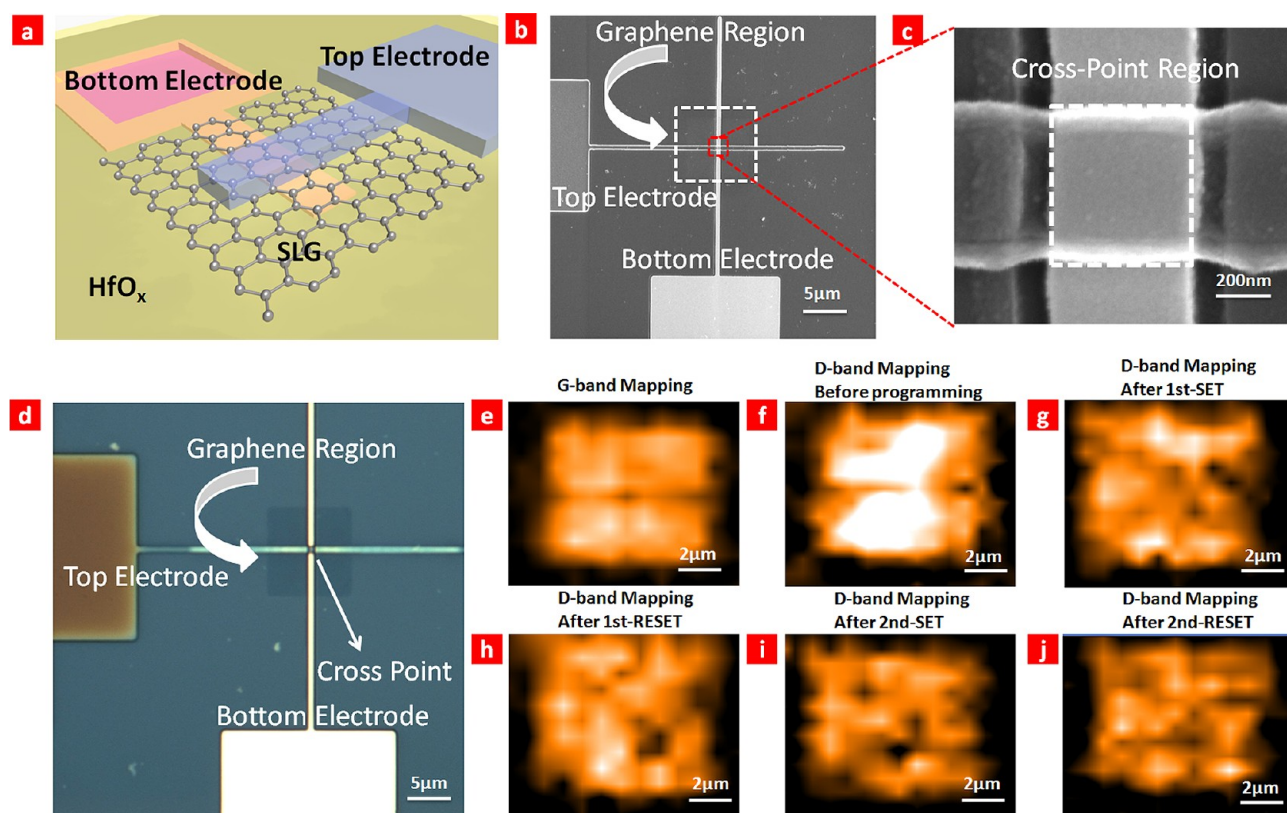


Figure 2. G-RRAM with crossbar structure and Raman mapping of SLG during consecutive electrical programming repeated for 2 cycles. (a) Schematic structure of G-RRAM with crossbar top and bottom electrodes. (b) A SEM image of $0.5 \times 0.5 \mu\text{m}^2$ cross-point region inside the $10 \times 10 \mu\text{m}^2$ SLG under low magnification. (c) A SEM image of $0.5 \times 0.5 \mu\text{m}^2$ cross-point region under high magnification. (d) An optical image of $0.5 \times 0.5 \mu\text{m}^2$ cross-point region inside the $10 \times 10 \mu\text{m}^2$ SLG. (e) The Raman G band intensity mapping. It shows the entire area of $10 \times 10 \mu\text{m}^2$ covered by graphene. (f–j) The Raman D band intensity area mapping for the first two SET/RESET programming cycles. It shows the D-band intensity decrease gradually during the programming cycles.

change of the 2D peak intensity with RRAM programming operation is consistently observed. Raman D-band intensity is sensitive to dangling bond (DB) defects in SLG. D peak can be reduced after thermal annealing, indicative of the restoration of the damaged lattice.³¹ As shown in Figure 2f–j and Figure 3b, D peak increases when defects are introduced to graphene material. The initial strong D peak in Figure 2f is mainly related to the defects in graphene, which may be introduced during the device fabrication (such as TiN sputtering). It is likely that the gradual reduction of the D peak (as shown in Figure 2g–j and Figure 3b) during the switching cycle is due to thermal annealing in the graphene. As a result of the reduction of the number of defects in the graphene by thermal annealing, the resistance of SLG could be reduced after the SET/RESET process.³²

G peak shift and 2D peak intensity change reflect the change of doping concentrations in graphene.³³ The doping mechanism in this case is investigated as follows: in G-RRAM, the sensitivity of G-peak position is monitored during program cycling. For example, the G-peak position after the first-SET is 1593 cm^{-1} , which indicates that the SLG is heavily p-type doped ($n \sim 5 \times 10^{12}/\text{cm}^{-2}$).³⁴ The G-peak position after the first-RESET is 1588 cm^{-1} , which indicates that the SLG is lighter p-type doped ($n \sim 2.5 \times 10^{12}/\text{cm}^{-2}$).³⁴ In G-RRAM, we also observed reversible shifts of G peak position with RRAM programming operations (Figure 3c). Figure 3d shows the intensity of 2D-peak as a function of switching cycle. The 2D peak intensity of SET is always lower than the RESET in each

cycle, and reversible changes of 2D peak intensity with RRAM programming actions are observed. It is possible that the G peak shift and the change of 2D peak intensity might result from the doping changes due to migration of oxygen ions: during SET process, oxygen ions escape from the oxide layer and diffuse laterally until they form covalent bonds with DB defects on SLG surface. This process would dope the graphene into p-type, which will shift the G-peak to larger wavenumber and decrease the intensity of the 2D-peak. When the oxygen ions are trapped by the SLG, the resistance of SLG could be reduced since the oxygen is a p-type dopant for graphene.³⁵ During the RESET process, oxygen ions move back to oxide layer due to the reversed applied electrical field. This process would change the graphene toward intrinsic doping, which will shift the G-peak to a smaller wavenumber and increase the intensity of the 2D-peak. When the oxygen ions are released from SLG, the resistance of SLG could be increased since the SLG becomes intrinsic.³⁵

Figure 4a shows the G-RRAM requires a higher forming voltage due to the built-in series resistance in G-RRAM. Because the inserted SLG increases the overall low resistance state (LRS) resistance for G-RRAM, a significant reduction of RESET current as compared to C-RRAM is observed (see Figure 4b) while using the same current compliances for G-RRAM and C-RRAM. As shown in Figure 4c, the average RESET current is reduced by 11 times. It should be noted in Figure 4d that the $10 \mu\text{A}$ SET compliance is not an optimized programming condition for C-RRAM since the resistance

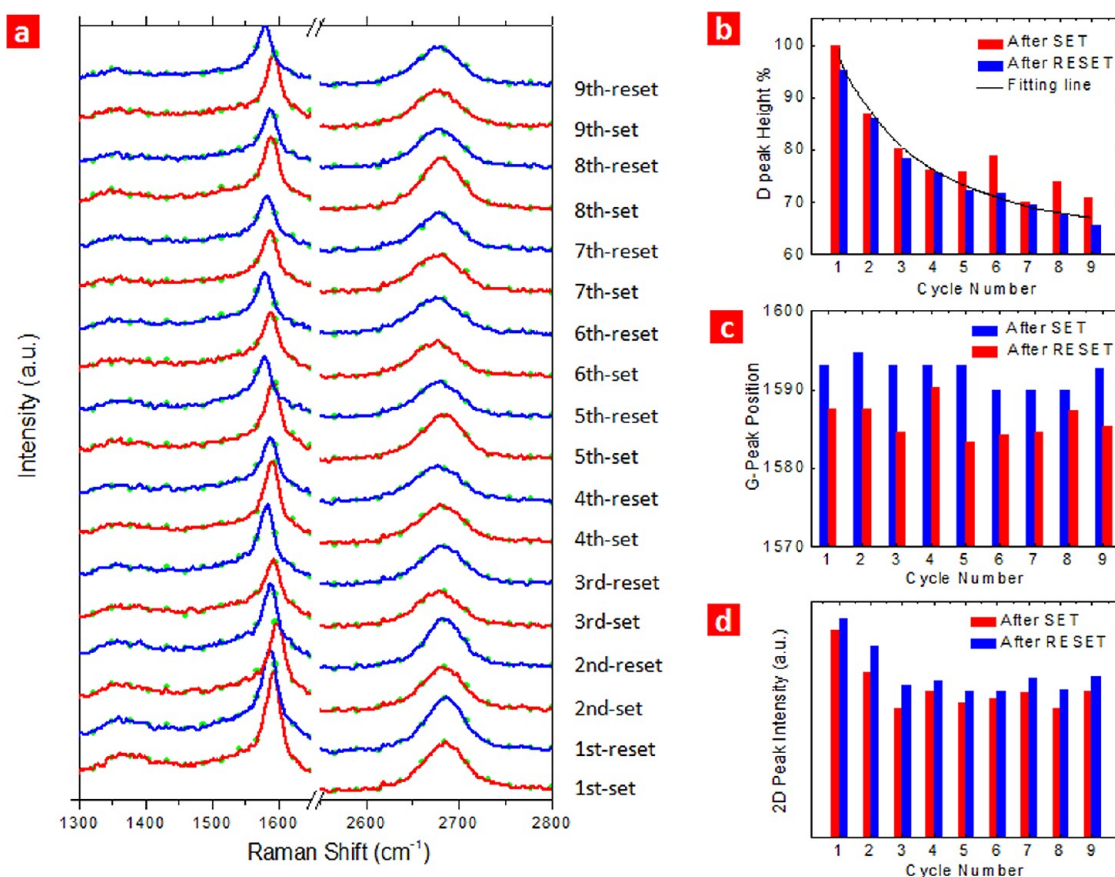


Figure 3. Single-point Raman measurements of SLG during consecutive electrical programming repeated for nine cycles. (a) Single-point Raman data measured after SET and RESET cycles at the same location, which is 1 μm from the cross-point. The dash lines mark the D, G, and 2D peak, which will be analyzed in (b–d). (b) Statistical analysis of D peak drop as a function of switching cycle. It is observed that the D peak gradually decreases. (c) The position of G peak as a function of switching cycle. The G-peak position of the SET is always higher than the RESET in each cycle, and reversible shifts of G peak position with RRAM programming actions are observed. (d) The intensity of 2D peak as a function of switching cycle. The 2D-peak intensity of the SET is always lower than the RESET in each cycle, and reversible changes of 2D peak intensity with RRAM programming events are observed.

window decays quickly. Therefore, in order to achieve stable switching, optimized larger compliance current of 100 μA is applied on the C-RRAM. As shown in Figure 4e, more significant reduction of RESET current is observed when both samples are switching under their optimal testing conditions (10 μA SET compliance for G-RRAM and 100 μA SET compliance for C-RRAM). In Figure 4f, the G-RRAM shows 22 times lower averaged RESET current compared to C-RRAM.

Figure 4g shows the resistance distribution of the two samples. G-RRAM device offers higher LRS resistance and better high resistance state (HRS) uniformity, both of which are important for RRAM as a memory device. Figure 4h shows the DC programming endurance data of G-RRAM. The LRS is quite uniform and is about 1 M Ω while the HRS shows large variations. The device cannot switch reliably with acceptable ratio of HRS to LRS after around 120 DC programming cycles. In general, HRS/LRS above 10 is preferred for practical memory application. Some emerging memory devices such as STT-RAM typically has ON/OFF resistance ratio of 2–6.³⁶ The worst case of G-RRAM window is about 6 (see Figure 4h), which is close to the minimum desired for memory application. It is observed that LRS is more uniform than HRS (as shown in Figure 4g). More effort is needed to improve the uniformity of HRS for G-RRAM. In Figure 4i, the programming power consumption (calculated as the product of RESET voltage and

RESET current) shows ~ 47 times reduction for G-RRAM as compared to C-RRAM. Retention measurements for the G-RRAM are shown in Supporting Information Figure S1. A retention time up to 10^5 seconds (which is equal to ~ 27.8 h) at 100 $^\circ\text{C}$ is achieved. The device also shows the potential for multilevel storage ability. The LRS resistance can be modulated by the SET compliance current by controlling the filament size (Supporting Information Figure S2). Good read immunity is achieved at a constant voltage stress of 0.3 V, which corresponds to 2×10^{10} endurance cycles of 50 ns READ pulse (Supporting Information Figure S3).

Inserting SLG into RRAM aims at achieving two goals: (1) limits oxygen migration further into the top electrode and serves as a monitor of the oxygen movement during SET and RESET programming; and (2) provides a high built-in series resistance to reduce RESET current and power consumption. Based on these observations, a model for the oxygen ions movement in G-RRAM emerges and this model is illustrated in Figure 5a. The diagrams represent (from left to right) elementary steps of the process including movement of oxygen ions to SLG during SET, capture of oxygen ions by SLG, movement of oxygen ions laterally on SLG, formation of covalent bond with SLG, followed by movement of oxygen ions back to HfO_x during RESET. The migration of the oxygen ions are aided by the Joule heating generated during the

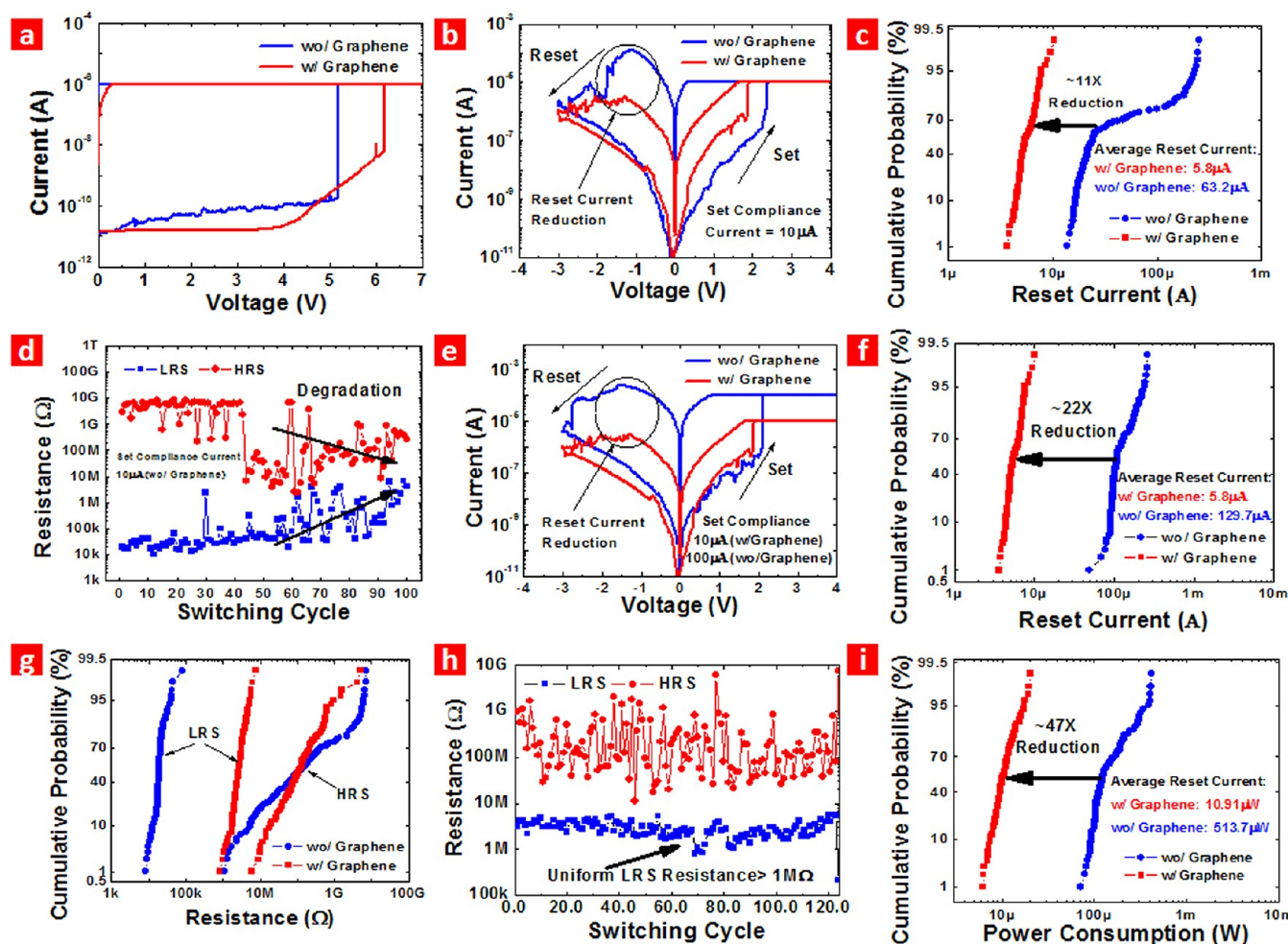


Figure 4. Electrical characterization of G-RRAM compared to C-RRAM. (a) Typical forming curve of G-RRAM and C-RRAM. (b) Typical resistive switching behavior of G-RRAM and C-RRAM. (c) Distribution of RESET currents of G-RRAM and C-RRAM obtained by 100 DC sweep cycles using $10\ \mu\text{A}$ as the SET current compliance. An ~ 11 times reduction of average RESET current is observed in G-RRAM. (d) DC sweep cycles of C-RRAM using $10\ \mu\text{A}$ as the SET current compliance. The degradation of resistance window margin indicates C-RRAM cannot switch stably under such small current compliance. (e) Typical resistive switching behavior of G-RRAM and C-RRAM using optimal testing conditions respectively. The 10 and $100\ \mu\text{A}$ current compliance are applied respectively to achieve steady switching. (f) Distribution of RESET currents of G-RRAM and C-RRAM obtained by 100 DC sweep cycles using the optimized switching parameters respectively. A reduction of up to 22 times of averaged RESET current is achieved. (g) Distribution of HRS/LRS resistances obtained by DC sweep in G-RRAM and C-RRAM. The LRS resistance of G-RRAM is ~ 100 times higher due to the insertion of SLG while the smaller resistance window is a trade off. (h) DC switching endurance of G-RRAM. The LRS resistance is increased to $>1\ \text{M}\Omega$ due to inserted SLG while the large variation of HRS resistance needs to be improved to achieve uniform HRS/LRS ratio. (i) Distribution of RESET power consumption of G-RRAM and C-RRAM obtained by 100 DC sweep cycles. Approximately 47 times reduction of power consumption is observed for G-RRAM.

programming event. Previous experimental^{37,38} and theoretical³⁹ studies indicate that SLG could be used as oxygen barrier layer and the oxygen are highly mobile on SLG. There is also experimental³⁵ evidence that oxygen can be used as an oxygen capturing layer. Oxygen could form a modest covalent bond with SLG and the bond can be reversible, which can make G-peak shift right and left. This is consistent with our experimental results of G-peak shift in Figure 3c,d. A model for comparing the oxygen ions movement in G-RRAM and C-RRAM are shown in Supporting Information Figure S4 and S5.

In order to investigate the mechanism for the Joule heating and the origin of the reset current reduction in G-RRAM (as compared to C-RRAM), electrical measurement coupled with numerical simulation are employed. Specific contact resistivity ($\sim 1.4 \times 10^{-5}\ \Omega\text{-cm}^2$) extracted from transmission line method (TLM) in Figure 5b indicates a good contact between SLG and the top electrode. Moreover, as shown in Figure 5c, the series

resistance comparison between G-RRAM and C-RRAM suggests that a high interfacial resistance may exist at the SLG/HfO_x interface, possibly related to the high out-of-plane resistance of SLG and poor interaction between the graphene and the metal oxide. Schematic view of the energy level alignment of the G-RRAM with Pt/HfO_x/SLG/Ti/TiN structure is shown in Supporting Information Figure S6. In the simulated temperature profile of filament formation in Figure 5d, the local high temperature at SLG/HfO_x interface in G-RRAM suggests the possibility of a thermal annealing effect (see details in Supporting Information discussion). It is reported that graphene annealing can reduce the D-peak significantly.³¹ Therefore, it is speculated that the gradual reduction of D-peak is due to thermal annealing in the graphene.

In summary, we insert SLG in the electrode/oxide interface to probe the oxygen movement in RRAM. The D-band area

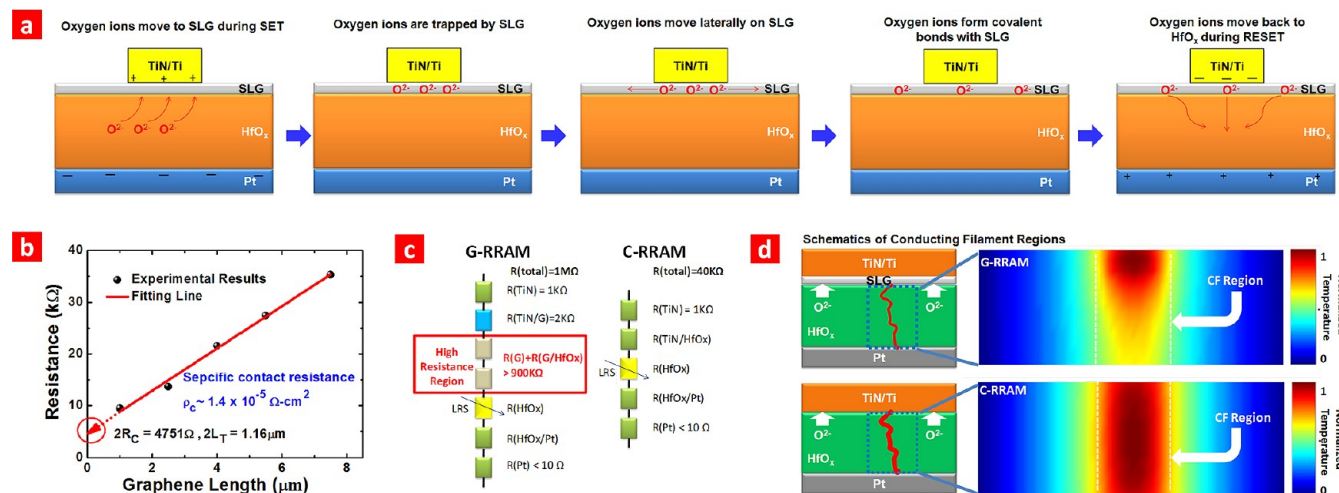


Figure 5. Theoretical analysis the oxygen movement and resistance in G-RRAM. (a) Schematic diagrams of the oxygen ions movement mechanisms in G-RRAM. The diagrams represent (from left to right) elementary steps of the process including movement of oxygen ions to SLG during SET, capture of oxygen ions by SLG, movement of oxygen ions laterally on SLG, formation of covalent bond with SLG, followed by movement of oxygen ions back to HfO_x during RESET. (b) Specific contact resistivity (ρ_c) of metal/SLG interface ($\sim 1.4 \times 10^{-5} \Omega\text{-cm}^2$) is extracted using TLM, indicating a good contact between SLG and metal electrode. In addition, the extracted value of ρ_c is close to the typical experimental data reported by other researchers, typically $10^{-5} \Omega\text{-cm}^2$. (c) Schematic comparison of series resistance across G-RRAM and C-RRAM respectively. The contact area is $1 \mu\text{m}^2$. It reveals that the high resistivity comes from SLG itself and the SLG/HfO_x interface. (d) Simulated temperature profile during the SET process for G-RRAM and C-RRAM, respectively.

map of SLG shows noticeable change during electric program cycling. This could be explained by the annealing effect in SLG,³¹ indicative of the restoration of damaged lattice. We also observe changes both in G-band shift and 2D-band intensity changing during repeated electric cycling. This observation might result from the doping effect by oxygen ion migration. During the SET process, oxygen ions escape from the oxide layer and diffuse laterally until they form covalent bonds with DB defects on SLG surface. During the RESET process, oxygen ions move back to oxide layer due to the applied electrical field in the opposite polarity. In addition, this inserted SLG design is shown to reduce RESET current and power consumption for the RRAM. This work indicates that SLG coupled with Raman spectroscopy could be a powerful and efficient method to investigate the oxygen movement in RRAM.

■ ASSOCIATED CONTENT

Supporting Information

Testing results and discussion of G-RRAM. This material is available free of charge via the Internet at <http://pubs.acs.org>.

■ AUTHOR INFORMATION

Corresponding Author

*E-mail: (T.-L.R.) RenTL@tsinghua.edu.cn; (Y.Z.) yzhang5@lbl.gov; (H.-S.P.W.) hspwong@stanford.edu.

Present Address

#Suzhou Institute of Nano-Tech and Nano-Bionics, Chinese Academy of Sciences, Suzhou 215123, China. E-mail: yzhang2012@sinano.ac.cn

Author Contributions

[†]These authors contributed equally to this work.

Notes

The authors declare no competing financial interest.

■ ACKNOWLEDGMENTS

The work done at Tsinghua is supported by National Natural Science Foundation (61025021, 60936002, 51072089, 61020106006) and National Key Project of Science & Technology (2009ZX02023-001-3, 2011ZX02403-002) of China. The graphene sample preparation, electrical and Raman characterizations of the RRAM devices were performed at the Molecular Foundry of Lawrence Berkeley National Laboratory, supported by the Office of Science, Office of Basic Energy Sciences, of the U.S. Department of Energy under contract no. DE-AC02-05CH11231. This work is supported in part by the member companies of the Stanford Non-Volatile Memory Technology Research Initiative (NMTRI). This work is done in part at the Stanford Nanofabrication Facility (SNF), a member of the NSF-supported National Nanotechnology Infrastructure Network (NNIN) and the Molecular Foundry at the Lawrence Berkeley National Laboratory. H.T. is additionally supported by the Ministry of Education Scholarship of China. S.Y. and J.L. are additionally supported by the Stanford Graduate Fellowship. B.G. is additionally supported in part by the Stanford School of Engineering China Research Exchange Program. The support of K.X. is very much appreciated. We are grateful for the discussions with Professor Zhenan Bao and Dr. Nan Liu from Stanford University.

■ REFERENCES

- (1) Wong, H. S. P.; et al. *Proc. IEEE* **2012**, *100*, 1951–1970.
- (2) Lee, H. Y.; et al. *IEEE Int. Electron Devices Meet.* **2010**, *19* (7), 4.
- (3) Govoreanu, B.; et al. *IEEE Int. Electron Devices Meet.* **2011**, *31* (6), 4.
- (4) Meyer, R.; Kohlstedt, H. *IEEE Trans. Sonics Ultrason.* **2006**, *53*, 2340–2348.
- (5) Liu, X.; et al. *J. Nanosci. Nanotechnol.* **2012**, *12*, 3252–3255.
- (6) Tseng, Y. H.; Shen, W. C.; Lin, C. J. *J. Appl. Phys.* **2012**, *111*, 73701–737015.
- (7) Son, J. Y.; Shin, Y. H.; Kim, H.; Jang, H. M. *ACS Nano* **2010**, *4*, 2655–2658.
- (8) Uenuma, M.; et al. *Nanotechnology* **2011**, *22*, 215201.

- (9) Magyari-Kope, B.; Tendulkar, M.; Park, S. G.; Lee, H. D.; Nishi, Y. *Nanotechnology* **2011**, *22*, 254029.
- (10) Son, J. Y.; Kim, C. H.; Cho, J. H.; Shin, Y. H.; Jang, H. M. *ACS Nano* **2010**, *4*, 3288–3292.
- (11) Park, G. S.; et al. *Appl. Phys. Lett.* **2007**, *91*.
- (12) Sakamoto, T.; et al. *Appl. Phys. Lett.* **2007**, *91*.
- (13) Yang, Y. C.; Pan, F.; Liu, Q.; Liu, M.; Zeng, F. *Nano Lett.* **2009**, *9*, 1636–1643.
- (14) Kwon, D. H.; et al. *Nat. Nanotechnol.* **2010**, *5*, 148–153.
- (15) Yang, Y.; et al. *Nat. Commun.* **2012**, *3*, 732.
- (16) Waser, R.; Aono, M. *Nat. Mater.* **2007**, *6*, 833–840.
- (17) Wang, S. Y.; Lee, D. Y.; Huang, T. Y.; Wu, J. W.; Tseng, T. Y. *Nanotechnology* **2010**, *21*, 495201.
- (18) Zhang, L.; et al. *Nanotechnology* **2011**, *22*, 254016.
- (19) Wu, X.; et al. *Nanotechnology* **2011**, *22*, 455702.
- (20) Novoselov, K. S.; et al. *Science* **2004**, *306*, 666–669.
- (21) Bolotin, K. I.; et al. *Solid State Commun.* **2008**, *146*, 351–355.
- (22) Lee, C.; Wei, X. D.; Kysar, J. W.; Hone, J. *Science* **2008**, *321*, 385–388.
- (23) Balandin, A. A.; et al. *Nano Lett.* **2008**, *8*, 902–907.
- (24) Bae, S.; et al. *Nat. Nanotechnol.* **2010**, *5*, 574–578.
- (25) Tian, H.; et al. *ACS Nano* **2011**, *5*, 4878–4885.
- (26) Tian, H.; et al. *Sci. Rep.* **2012**, *2*, 523.
- (27) Hong, A. J.; et al. *ACS Nano* **2011**, *5*, 7812–7817.
- (28) Li, Y.; Sinitskii, A.; Tour, J. M. *Nat. Mater.* **2008**, *7*, 966–971.
- (29) Liu, L.; et al. *Nano Lett.* **2008**, *8*, 1965–1970.
- (30) Shin, D.-W.; et al. *ACS Nano* **2012**, *6*, 7781–7788.
- (31) Lin, Y. C.; Lin, C. Y.; Chiu, P. W. *Appl. Phys. Lett.* **2010**, *96*.
- (32) Cheng, Z. G.; et al. *Nano Lett.* **2011**, *11*, 767–771.
- (33) Das, A.; et al. *Nat. Nanotechnol.* **2008**, *3*, 210–215.
- (34) Yan, J.; Zhang, Y.; Kim, P.; Pinczuk, A. *Phys. Rev. Lett.* **2007**, *98*, 166802.
- (35) Ryu, S.; et al. *Nano Lett.* **2010**, *10* (12), 4944–4951.
- (36) Chen, E.; et al. *IEEE Trans. Magn.* **2010**, *46*, 1873–1878.
- (37) Bunch, J. S.; et al. *Nano Lett.* **2008**, *8*, 2458–2462.
- (38) Stolyarova, E.; et al. *Nano Lett.* **2009**, *9*, 332–337.
- (39) Ito, J.; Nakamura, J.; Natori, A. *J. Appl. Phys.* **2008**, *103*.